

RESEARCH ARTICLE | JULY 20 2017

Differential carrier lifetime and transport effects in electrically injected III-nitride light-emitting diodes **FREE**

A. Rashidi ; M. Nami ; M. Monavarian; A. Aragon; K. DaVico; F. Ayoub; S. Mishkat-UI-Masabih; A. Rishinaramangalam; D. Feezell



J. Appl. Phys. 122, 035706 (2017)

<https://doi.org/10.1063/1.4994648>

 CHORUS



Articles You May Be Interested In

Differential carrier lifetime in InGaN-based light-emitting diodes obtained by small-signal frequency-domain measurements

J. Appl. Phys. (January 2017)

Study on efficiency droop in InGaN/GaN light-emitting diodes based on differential carrier lifetime analysis

Appl. Phys. Lett. (January 2016)

Impact of crystal orientation on the modulation bandwidth of InGaN/GaN light-emitting diodes

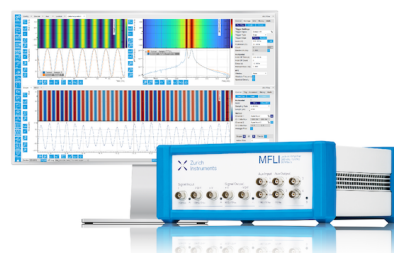
Appl. Phys. Lett. (January 2018)

Challenge us.

What are your needs for periodic signal detection?



Find out more



Differential carrier lifetime and transport effects in electrically injected III-nitride light-emitting diodes

A. Rashidi,^{1,a)} M. Nami,¹ M. Monavarian,¹ A. Aragon,¹ K. DaVico,¹ F. Ayoub,² S. Mishkat-Ui-Masabih,¹ A. Rishinaramangalam,¹ and D. Feezell^{1,2}

¹Center for High Technology Materials (CHTM), University of New Mexico, Albuquerque, New Mexico 87106, USA

²Electrical and Computer Engineering Department, University of New Mexico, Albuquerque, New Mexico 87106, USA

(Received 9 May 2017; accepted 6 July 2017; published online 20 July 2017)

This work describes a small-signal microwave method for determining the differential carrier lifetime and transport effects in electrically injected InGaN/GaN light-emitting diodes (LEDs). By considering the carrier diffusion, capture, thermionic escape, and recombination, the rate equations are used to derive an equivalent small-signal electrical circuit for the LEDs, from which expressions for the input impedance and modulation response are obtained. The expressions are simultaneously fit to the experimental data for the input impedance and modulation response for nonpolar InGaN/GaN micro-LEDs on free-standing GaN substrates. The fittings are used to extract the transport related circuit parameters and differential carrier lifetimes. The dependence of the parameters on the device diameter and current density is reported. We also derive approximations for the modulation response under low and high injection levels and show that the transport of carriers affects the modulation response of the device, especially at low injection levels. The methods presented are relevant to the design of high-speed LEDs for visible-light communication. Published by AIP Publishing. [<http://dx.doi.org/10.1063/1.4994648>]

I. INTRODUCTION

High-speed InGaN/GaN light-emitting diodes (LEDs) are of recent interest for visible-light communication (VLC) in future light-fidelity (Li-Fi) networks.¹ As a compliment to traditional radio frequency (RF) technology, VLC systems can achieve multi-Gb/s data rates by modulating LEDs, which function as illumination and communication sources simultaneously. When combined with multiplexing techniques and advanced modulation schemes, VLC systems have been demonstrated with 10 Gb/s data rates.^{2,3} In addition to Li-Fi networks, high-speed visible-emitting LEDs also have application in polymer optical fiber communication (POF)⁴ and underwater wireless optical communication (UWOC).⁵ Because the bandwidth of conventional broad-area LEDs used for lighting is limited to tens of MHz, micro-LEDs have been developed to achieve the higher bandwidths needed for VLC applications.^{6–9} In general, higher bandwidth is achieved by reducing both the transport-related time constants (i.e., RC effects) of the device and the differential carrier lifetime. Micro-LEDs exhibit smaller parasitic capacitance and allow for operation at higher carrier densities where the differential carrier lifetime is reduced.¹⁰ However, the reduction in carrier lifetime is also accompanied by efficiency droop at high carrier densities, and the dependence of the transport effects on device geometry and structure remains the subject of investigation.¹¹

To better optimize micro-LEDs for speed and efficiency, characterization methods are needed to quantify the differential carrier lifetime and the transport-related time constants

as a function of carrier density for a variety of epitaxial structures and device geometries. The ideal characterization method should be performed under electrical injection to represent actual LED operating conditions. Studies of the carrier lifetime also aid in the understanding of fundamental material issues in III-nitrides such as efficiency droop^{12–14} and green gap.^{15,16} Methods to decouple the carrier lifetime and transport-related time constants also provide information about the factors limiting the modulation bandwidth.

Time resolved photoluminescence (TRPL) has conventionally been used to measure carrier lifetime by tracking the decay in photoluminescence intensity as a function of time for different optical pumping densities.^{17–21} The carrier lifetime is then extracted by fitting the data to a mono-exponential or bi-exponential decay model.¹⁹ While TRPL measurements are well established, several limitations exist with this technique for characterizing electrically injected devices. First, TRPL is performed under optical pumping, where the carrier density is difficult to quantify unless the detailed absorption properties of the active region are known. Second, TRPL typically assumes uniform pumping of the active region, neglecting carrier transport effects.²² Third, TRPL does not achieve the flat-band conditions achieved under electrical injection, resulting in a different electron-hole wavefunction overlap.²³ Fourth, TRPL yields the *carrier lifetime*, but not the *differential carrier lifetime*. The differential carrier lifetime represents the response to a small signal and depends upon the local slope of the recombination vs. carrier density curve (dR/dN). The differential carrier lifetime is typically a factor of 2–3 times smaller than the carrier lifetime.²⁴ This distinction is important because the

^{a)}Electronic mail: arashidi@unm.edu

small-signal modulation bandwidth is more closely related to the differential carrier lifetime. Finally, TRPL does not provide information about the transport effects in the device. Thus, the TRPL method provides an incomplete picture for characterizing electrically injected LEDs.

To more accurately characterize the differential carrier lifetime in electrically injected LEDs under typical operating conditions, small-signal RF methods have previously been used. An earlier method applied a time-variant small-signal modulation to a DC signal and tracked the phase difference between the input electrical signal and the modulated light output of the LED.^{25,26} One limitation of this method is the assumption that the frequency modulation bandwidth is only governed by the carrier recombination process,^{14,27} while studies have shown it is also affected by carrier transport.^{28–30} An alternative method to extract the carrier lifetime involves the fitting of the small-signal impedance characteristics to simple circuit models representing only the active region of the LED.^{22,26,31} However, by using extracted parameters from only the impedance data, one cannot reconstruct the modulation response of the device. In addition, more recent simulations have shown that transport effects should also be considered in the circuit model.³² David *et al.* recently included transport effects using a similar method to study the temperature dependence of carrier recombination and introduced coulomb-enhanced capture as a new process in *c*-plane InGaN LEDs.³³

In this work, using a rate equation approach, we derive a small-signal equivalent circuit for III-nitride LEDs considering both recombination and transport effects. The input impedance and modulation response of the circuit are simultaneously fit to the impedance and modulation response data of nonpolar InGaN/GaN LEDs on free-standing GaN. Nonlinear regression is used to achieve excellent fittings to the RF data without pre-defining or assuming any parameters based on DC measurements. The complete modulation response and impedance characteristics are reconstructed from the model. The differential carrier lifetime and transport related parameters are obtained as a function of current density for four different micro-LED sizes. We then derive approximations for the modulation response under low and high injection levels and show that the transport of carriers affects the modulation response of the device. Only considering the recombination process for predicting the modulation response introduces deviations from the full model, especially at low injections. Additionally, at high current densities, we separate the differential carrier lifetime and define an RC time constant related to transport effects. Decoupling the effects of transport and recombination on the modulation response is important to establish device designs with low RC time constant and short recombination lifetime, which are both needed for high-speed VLC applications.

II. DEVICE STRUCTURE

The LEDs studied were grown on a nonpolar (*m*-plane) free-standing GaN substrate by metal organic chemical vapor deposition (MOCVD). The structure consists of $\sim 2\text{-}\mu\text{m}$ -thick *n*-doped GaN ($[\text{Si}] = 4 \times 10^{17} \text{ cm}^{-3}$), $\sim 100\text{ nm}$ of highly

doped *n*-GaN ($[\text{Si}] = 6 \times 10^{18} \text{ cm}^{-3}$), three pairs of undoped InGaN (6 nm)/GaN (15 nm) quantum wells, $\sim 100\text{ nm}$ of moderately doped *p*-GaN ($[\text{Mg}] = 3 \times 10^{19} \text{ cm}^{-3}$), and a 15 nm highly doped *p*++-GaN ($[\text{Mg}] = 1 \times 10^{20} \text{ cm}^{-3}$). The devices were fabricated with circular mesa diameters of 50, 60, 70, and 80 μm . A 200-nm-thick ITO layer was deposited on the device to serve as the *p*-contact and aid in current spreading across the mesa. The details of the growth and fabrication process have previously been reported elsewhere.⁹ A schematic diagram of the device is shown in Fig. 1.

III. SMALL-SIGNAL CIRCUIT MODEL

For obtaining the small-signal equivalent circuit of the LEDs, the single-particle rate equations describing the dynamics of electron-hole pairs are used. The approach used follows that in Ref. 34. Excellent agreement between the theory and experiment justifies the assumption of using single-particle rate equations in this sample. For asymmetric energy band diagram structures in which the behavior of holes and electrons are significantly different, one can use general two-particle rate equations, which requires the analysis of four nonlinear coupled rate equations.³⁵ We also assume that the lateral carrier distribution is uniform both in the cladding and the MQW layers. Figure 2 shows the energy band diagram and dominant carrier processes in the LED structure. Carriers are injected from the metal contacts into the cladding region. A small portion of the injected current must charge the space charge capacitance (C_{sc}) to compensate the built-in voltage of the *p*-*i*-*n* junctions. $C_{sc} \frac{dV_c}{dt}$ is the required current to charge C_{sc} , while V_c is the junction voltage. Carriers in the cladding region diffuse toward the MQW layers under forwarding bias with a time delay of τ_{diff} and are captured by the quantum wells (QWs) with a capture rate of τ_{cap} . The spontaneous emission of carriers in the cladding region is neglected. The total delay experienced by unconfined carriers in the cladding (N_c) region is defined as the cladding delay $\tau_c = \tau_{diff} + \tau_{cap}$. After capture by the QWs, the carrier population in the MQW (N_w) can be altered by two processes: recombination (radiative and non-radiative), with rate τ_{rec} , and thermionic emission to the cladding region, with rate τ_{esc} . Any effects of transport of carriers between the quantum wells are folded into the carrier recombination lifetime. Therefore, the rate equations governing the

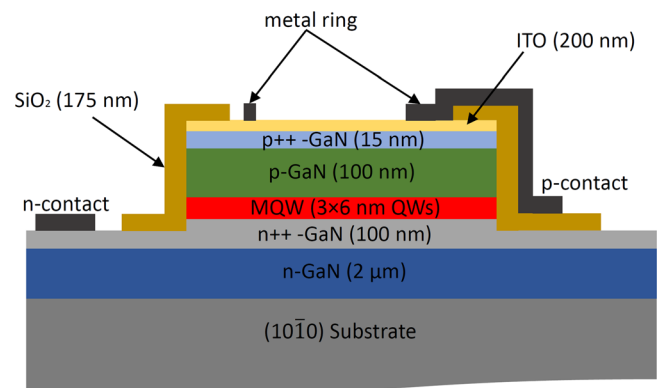


FIG. 1. Schematic diagram of the circular mesa LED.

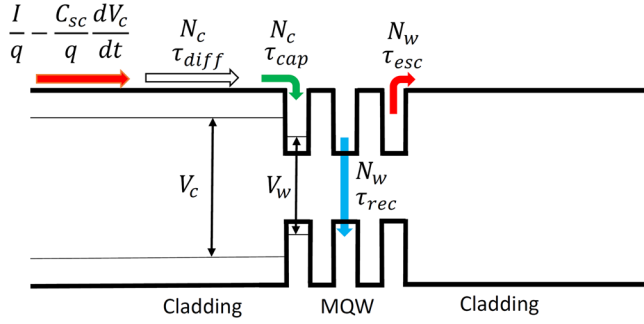


FIG. 2. Energy band diagram of nonpolar InGaN/GaN LED under flat band condition. Carriers experience general processes of capture, escape, and recombination in the QW.

carrier population in the cladding and MQW regions can be written as follows:

$$\frac{dN_c}{dt} = \frac{I}{q} - \frac{C_{sc}}{q} \frac{dV_c}{dt} + \frac{N_w}{\tau_{esc}} - \frac{N_c}{\tau_c}, \quad (1a)$$

$$\frac{dN_w}{dt} = -\left(\frac{1}{\tau_{rec}} + \frac{1}{\tau_{esc}}\right)N_w + \frac{N_c}{\tau_c}. \quad (1b)$$

A. Small-signal rate equations

In Fig. 2, V_c and V_w are defined as the voltages associated with the quasi-Fermi level difference across the cladding region and the MQW, respectively. The quasi-Fermi level associated with the carriers in the cladding is assumed to be flat throughout the region and determined by the applied voltage.³⁶ Parasitic effects of the device are ignored now but will be added to the intrinsic equivalent circuit later. V_c can be related to the carrier population through Boltzmann statistics by

$$N_c \propto e^{\frac{V_c}{mV_T}}. \quad (2)$$

Here, N_c is the total number of carriers in the cladding region. $V_T = KT/q$, where K and T are the Boltzmann constant and absolute temperature, respectively, q is the electron charge, and m is the ideality factor of the diode. The small-signal bias added to the DC causes a small perturbation of the carrier number in the cladding and MQW regions around their steady state value, which leads to the linearization of Eq. (2) as follows:

$$N_{c0} \propto e^{\frac{V_{c0}}{mV_T}}, \quad (3a)$$

$$N_c(\omega) \propto e^{\frac{V_{c0} + v_c(\omega)}{mV_T}}, \quad (3b)$$

$$N_c(\omega) \approx N_{c0} \left[1 + \frac{v_c(\omega)}{mV_T} \right], \quad (3c)$$

$$N_c(\omega) \approx N_{c0} + \frac{N_{c0}v_c(\omega)}{mV_T}. \quad (3d)$$

Here, parameters, with subscript 0 refer to the steady state value. $v_c(\omega)$ is the small-signal voltage applied to the cladding region. The second term in Eq. (3d) is the total number of perturbed carriers associated with the small-signal voltage in the cladding region and is defined as $n_c(\omega)$. Therefore, the

perturbed carrier number is proportional to both the small-signal bias and the steady state total number of carriers. Therefore, using Eq. (3d) we can write

$$v_c(\omega) = \frac{qn_c(\omega)}{C_c}, \quad (4a)$$

$$\text{where } C_c = \frac{qN_{c0}}{mV_T}. \quad (4b)$$

C_c is the capacitance associated with the unconfined carriers in the cladding region. Using an analogous approach, the quasi-Fermi level separation related to the small-signal modulation in the MQW region is the small-signal charge due to the perturbed number of carriers in the MQW region divided by their associated capacitance

$$v_w(\omega) = \frac{qn_w(\omega)}{C_w}, \quad (5)$$

where $n_w(\omega)$ is small-signal perturbation of the carrier population in the MQW region. As with C_c , C_w is defined as the capacitance associated with the confined carriers in the MQW.

To derive the intrinsic equivalent electrical circuit, and hence, the intrinsic impedance and modulation response of the LED, the rate equations (1a) and (1b) are written in their small-signal form by assuming a small-signal value in addition to steady state for all variables. For example, $I = I_0 + i(\omega)e^{j\omega t}$, $N_c = N_{c0} + n_c(\omega)e^{j\omega t}$, $N_w = N_{w0} + n_w(\omega)e^{j\omega t}$, $V_c = V_{c0} + v_c(\omega)e^{j\omega t}$, and $V_w = V_{w0} + v_w(\omega)e^{j\omega t}$. After insertion of these expressions into Eqs. (1a) and (1b), the small-signal rate equations become

$$j\omega n_w(\omega) = -\left[\frac{1}{\tau_{rec}} + \frac{1}{\tau_{esc}}\right]n_w(\omega) + \frac{n_c(\omega)}{\tau_c}, \quad (6a)$$

$$j\omega n_c(\omega) = \frac{i(\omega)}{q} - j\omega v_c(\omega) \frac{C_{sc}}{q} + \frac{n_w(\omega)}{\tau_{esc}} - \frac{n_c(\omega)}{\tau_c}, \quad (6b)$$

where $i(\omega)$ is the modulating injected current. Using Eqs. (4a) and (5), Eqs. (6a) and (6b) can be re-written based on $v_c(\omega)$ and $v_w(\omega)$, which results in the following equations in matrix format:

$$\begin{pmatrix} j\omega C_w + \frac{C_w}{\tau_{rec}} + \frac{C_w}{\tau_{esc}} & -\frac{C_c}{\tau_c} \\ -\frac{C_w}{\tau_{esc}} & j\omega(C_c + C_{sc}) + \frac{C_c}{\tau_c} \end{pmatrix} \begin{pmatrix} v_w(\omega) \\ v_c(\omega) \end{pmatrix} = \begin{pmatrix} 0 \\ i(\omega) \end{pmatrix}. \quad (7)$$

We further define

$$R_c = \frac{\tau_c}{C_c} \quad (8a)$$

and

$$R_w = \frac{\tau_{rec}}{C_w} \quad (8b)$$

as the resistance due to carriers in the cladding and MQW regions, respectively. According to linear circuit theory, matrix equation (7) is associated with an equivalent electrical circuit for the LED, which has two nodes (in addition to the

ground node).³⁷ This equation also requires the non-diagonal elements of the admittance matrix of the circuit to be equal. This implies $-\frac{C_c}{\tau_c} = -\frac{C_w}{\tau_{esc}} = -\frac{1}{R_c}$, which leads to

$$\tau_{esc} = R_c C_w \quad (9a)$$

and

$$C_w = C_c \frac{\tau_{esc}}{\tau_c}. \quad (9b)$$

Based on these new definitions, (7) can be written as

$$\begin{pmatrix} j\omega C_w + \frac{1}{R_w} + \frac{1}{R_c} & -\frac{1}{R_c} \\ -\frac{1}{R_c} & j\omega(C_c + C_{sc}) + \frac{1}{R_c} \end{pmatrix} \begin{pmatrix} v_w(\omega) \\ v_c(\omega) \end{pmatrix} = \begin{pmatrix} 0 \\ i(\omega) \end{pmatrix}. \quad (10)$$

$$\frac{v_{out}(\omega)}{v_{in}(\omega)} = \frac{R_w}{R_s(1 + j\omega\tau_{rec})(1 + j\omega\tau_0) + R_s(j\omega R_w C_{tot}) + R_c(1 + j\omega\tau_{rec}) + R_w}, \quad (12)$$

where $C_{tot} = C_c + C_{sc}$ and $\tau_0 = R_c C_{tot} = \tau_c + R_c C_{sc}$. τ_0 is referred to as the diode time constant.

B. Steady-state rate equations

The steady state solutions to Eqs. (1a) and (1b) result in the following equations:

$$N_{c0} = \frac{I_0}{q} \tau_c \left[1 + \frac{\tau_{rec}}{\tau_{esc}} \right], \quad (13a)$$

$$N_{w0} = \frac{I_0}{q} \tau_{rec}, \quad (13b)$$

R_c and R_w can also be derived using (13a), (4b), (8a), (8b), and (9b), resulting in

$$R_c = \frac{mV_T}{I_0} \left[\frac{1}{1 + \frac{\tau_{rec}}{\tau_{esc}}} \right], \quad (14a)$$

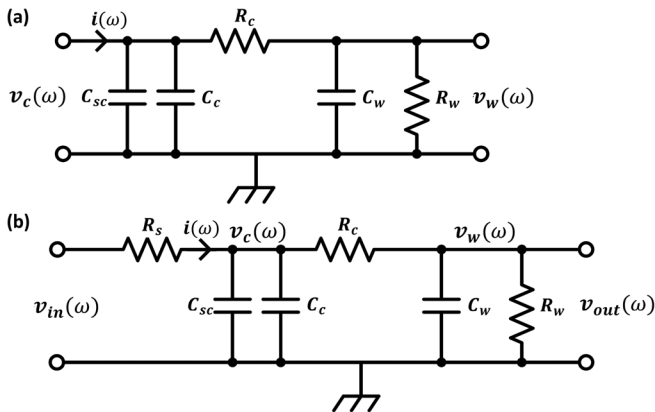


FIG. 3. (a) The small-signal intrinsic equivalent circuit of the LED. (b) The intrinsic equivalent circuit of the LED with parasitic elements added.

The admittance matrix in (10) yields the small-signal intrinsic equivalent circuit of the LED shown in Fig. 3(a). For including parasitic effects due to the finite conductance of the semiconductor cladding layers and semiconductor-metal contacts, a series resistance R_s can be added to the intrinsic equivalent circuit of the LED as shown in Fig. 3(b). The intrinsic impedance ($Z_{in}(\omega)$) and intrinsic modulation response of the LED can be derived from (10) as $\frac{v_c(\omega)}{i(\omega)}$ and $\frac{v_w(\omega)}{v_c(\omega)}$, respectively. The effect of R_s can be added to both intrinsic responses. Equations (11) and (12) are the total input impedance and modulation response of the LED structure, respectively

$$Z_{in}(\omega) = R_s + \frac{R_c(1 + j\omega\tau_{rec}) + R_w}{(1 + j\omega\tau_{rec})(1 + j\omega\tau_0) + j\omega C_{tot}R_w}, \quad (11)$$

$$R_w = \frac{mV_T}{I_0} \frac{1}{\left[1 + \frac{\tau_{esc}}{\tau_{rec}} \right]}. \quad (14b)$$

Here, it can be seen that $R_c + R_w = \frac{mV_T}{I_0}$, which is equal to the differential diode resistance R_d . It can also be seen from Fig. 3(a) that $R_d = Z_i(0)$, where $Z_i(\omega)$ is the intrinsic input impedance of the LED.

IV. EXPERIMENTAL RESULTS

The LEDs were biased at various DC densities and modulated with a small-signal voltage (100 mV) provided by port 1 of a network analyzer (NA) (Agilent PNA-X N5247A). The frequency of the small signal was swept from 10 MHz to 1 GHz. The LEDs were probed using a micro-RF ground-signal-ground probe (ACP40-GSG-150, Cascade Microtech, Inc.) and the modulated output light was fiber coupled and collected into a high-speed photodetector (DET025AFC, Thorlabs, Inc.). A low noise amplifier (PE15A1009, Pasternack Enterprises) was used to amplify the signal received by the photodetector, which was then coupled to port 2 of the NA to determine the modulation response (S_{21}). The real and imaginary parts of the impedance were extracted from the measured reflection coefficient (S_{11}), which was collected over the same frequency range as S_{21} . These measurements were carried out for devices with circular diameters of 50, 60, 70, and 80 μm and for current densities ranging from 20 A/cm² to 3 kA/cm².

Equations (11) and (12) may be simultaneously fit to the measured impedance data and modulation response to achieve a unique solution for the shared unknown parameters in the circuit model. Previous works have reported the fitting of only impedance data, where the reconstructed modulation response using impedance fitting is not the same as measured modulation response.^{22,26,31} The reason for the discrepancy is that

previously used simple parallel RC models represent a single-pole system, where the RC and carrier responses are lumped into a single lifetime. This simple model does not enable reconstruction of both the impedance and modulation responses. However, any accurate model for the LED should represent both the impedance and modulation responses. Here, we use rate equations to derive a more comprehensive model for the LED, which is more accurately represented by a two-pole system, where the RC and carrier responses are decoupled. In the two-pole system, the modulation response must be fit simultaneously with the impedance response to ensure a unique fit to both the measured impedance and modulation responses. If only the impedance response is fit, the modulation response for the two-pole system cannot be accurately reconstructed. When the two-pole model is simultaneously fit to both the impedance and modulation responses, the improvements include: (1) a unique solution is achieved for both the impedance and modulation responses, (2) both responses can be reconstructed from the model, and (3) more accurate values are obtained for the circuit elements. The impedance and modulation responses of the device, are therefore, measured at the same time. Simultaneously, the real and imaginary parts of Eq. (11) are fit to the impedance data, and the square of Eq. (12) is fit to the modulation response [i.e., the electrical power received by the NA in Fig. 4(b)]. Here, $20 \log(v_{out}(\omega)/v_{in}(\omega)) = 10 \log(p_{out}(\omega)/p_{in}(\omega))$, where p_{in} and p_{out} are the electrical powers transmitted and received at ports 1 and 2 of the NA, respectively. By using this method, both the impedance and modulation response can be reconstructed by the obtained parameters. Nearly perfect fittings with high R-squared values of above 0.95 were achieved, from which the parameters in the circuit model can be found. Figures 4(a) and 4(b) show examples of the simultaneous fitting of Eqs. (11) and (12) to the impedance and modulation response data, respectively.

A. Diode resistance and capacitance

Figures 5(a) and 5(b) show R_c and $C_c + C_{sc}$ as derived from the fittings for the LEDs operating at various current

densities. An inverse relation between R_c and the bias current is observed, which agrees with the relation derived earlier in Eq. (14a). According to Fig. 5(b), the capacitance at very low current densities is almost constant. This approximately constant capacitance is assumed to be the space charge capacitance of the diode. However, with increasing bias current, the capacitance due to diffusion and capture of carriers becomes dominant. We also observe that both R_c and $C_c + C_{sc}$ scale with the diode area as expected, with the resistance decreasing and the capacitance increasing for larger diameter LEDs.

B. Parasitic series resistance

Figure 6 shows the parasitic series resistance for the LEDs operating at various current densities. Two aspects of the series resistance dependence on device size and current density are notable. The series resistance generally increases for smaller diameter LEDs as expected, but the resistance for the 50 μm device is markedly higher than the devices of larger diameter. We attribute this to non-linear scaling of the various resistance components with diameter. For example, the parasitic series resistance depends upon the contact resistance, *p*-GaIn diameter, and *n*-GaIn area and thickness. We also note that the parasitic series resistance exhibits a weak dependence on current density. This may be attributed to non-ohmic contacts, which show reduced resistance at higher current densities, and to current crowding at higher current densities.³⁸

C. Lifetimes and time constants

Figure 7(a) shows the extracted carrier recombination lifetimes (τ_{rec}) and diode time constants (τ_0) for the LEDs at various current densities. The carrier lifetime decreases with increasing current (carrier) density due to the increase in the recombination rate with carrier density. This behavior is in good agreement with an ABC model describing carrier loss mechanisms in GaN devices.²⁶ The differential carrier lifetimes extracted for these nonpolar micro-LEDs range from

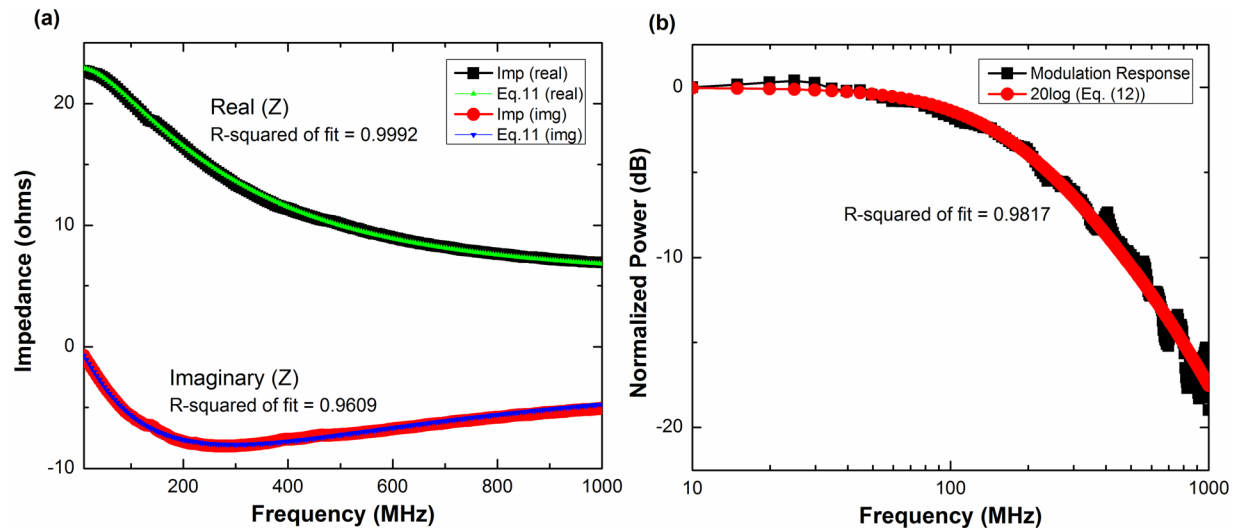


FIG. 4. Simultaneous fitting of (a) real and imaginary parts of Eq. (11) to the impedance data and (b) $20 \log [Eq. (12)]$ to the measured modulation response of a 70- μm -diameter device at a current density of 1 kA/cm^2 .

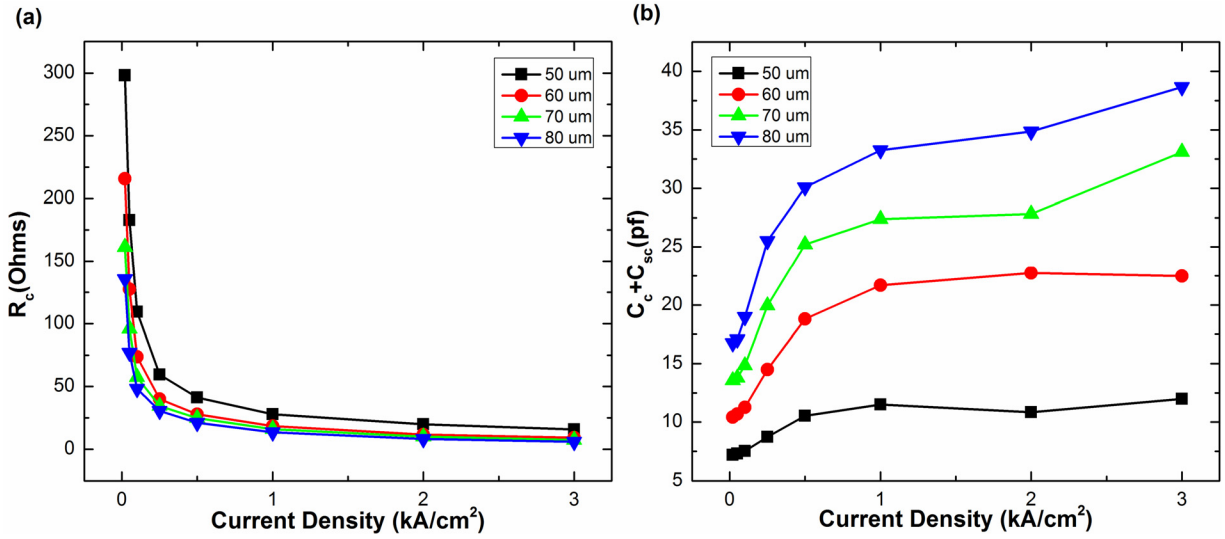


FIG. 5. (a) R_c , the resistance due to the unconfined carriers in the cladding region and (b) $C_c + C_{sc}$, the total capacitance of the unconfined carriers in the cladding and space charge regions for devices of different diameters at various current densities.

~ 5 ns at 20 A/cm^2 to ~ 0.87 ns at 3 kA/cm^2 . In electrically injected c-plane LEDs, differential carrier lifetimes ranging from 20 ns at 10 A/cm^2 to 5 ns at 100 A/cm^2 , 15 ns at 16 A/cm^2 to 2 ns at 320 A/cm^2 , and 2770 ns at 0.016 A/cm^2 to 367 ns at 12.9 A/cm^2 have been reported by David *et al.*,³³ Meneghini *et al.*,³⁹ and Riuttanen *et al.*,³¹ respectively. Although all the devices have the same active region, the differential carrier lifetimes are not the same for each device diameter. Larger diameters exhibit shorter lifetimes and higher modulation bandwidths. This remains the subject of investigation but may be due to non-uniform current spreading in larger diameter devices, which causes the effective current density to be higher in regions close to the metal pads, thus reducing the carrier lifetime.³⁸

According to Fig. 7(a), the diode time constant is 2–3 times shorter than the recombination lifetime. The diode time constant decreases with drive current density because in

$\tau_0 = R_c(C_c + C_{sc})$, R_c is inversely proportional to the drive current, while $C_c + C_{sc}$ has a weaker dependence on current, per Fig. 5. We also observe that the diode time constant scales with the diode diameter as expected, with smaller diameters having lower diode time constant.

Figure 7(b) shows the escape time constant of carriers from the QW. According to Eq. (9a), the escape time constant is dependent on carriers in both the cladding and MQW regions through R_c and C_w , respectively. According to Fig. 7(a), at very low current densities, before the flat band condition has been achieved, the number of carriers in the QWs is very low, resulting in long recombination and escape lifetimes (small rates). As the current density increases, the space-charge capacitance is gradually charged, R_s rapidly decreases, and more carriers enter the QWs, resulting in shorter recombination and escape lifetimes (larger rates). Once the space charge capacitance is charged, and the flat-band condition is achieved, carriers flood the QWs, and the recombination rate saturates. At even higher current densities, the escape time again increases, which was previously observed in GaAs-based devices.⁴⁰ The increase in the escape time at high current density is attributed to Coulomb forces between unconfined carriers in the cladding and confined carriers in the MQW region, which results in re-capture of some of the emitted carriers by the QWs, decreasing the overall escape rate. This phenomena was recently discussed by David *et al.*³³

D. Modulation response

To further investigate the modulation response of these devices and determine the limiting factors in the 3 dB bandwidth, deeper study of the transfer function is needed. Here, we propose approximations for low and high current density regimes and substantiate these approximations by comparing them to experimental data. The modulation response of the LED in Eq. (12) can be rearranged and written in the form of Eq. (15) as

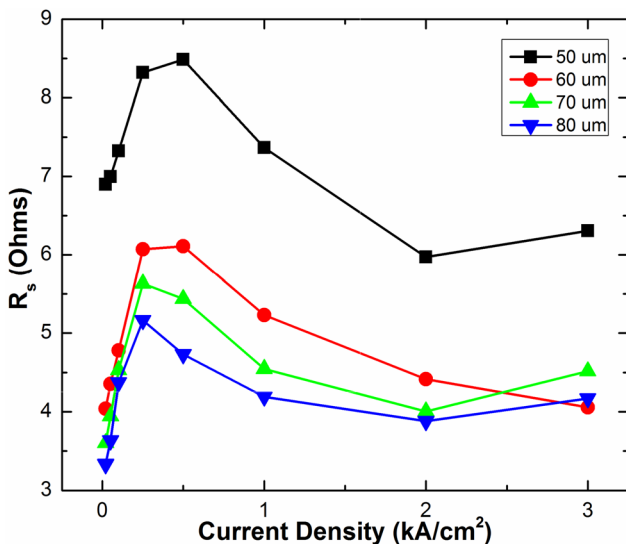


FIG. 6. Parasitic resistance due to the p and n -GaIn layers and metal pads for different device diameters.

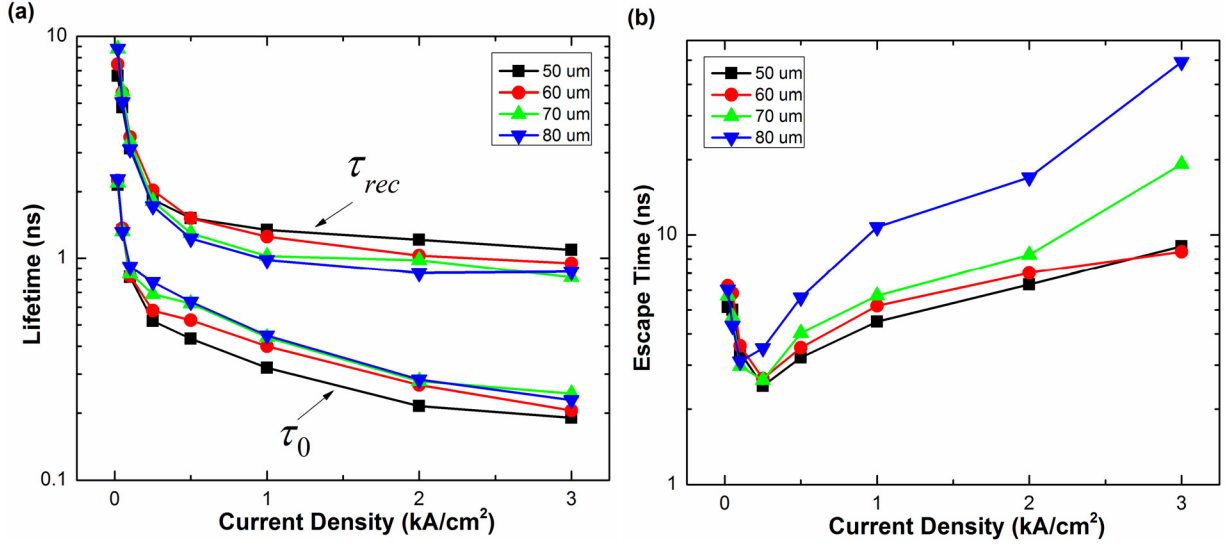


FIG. 7. (a) Differential carrier lifetime and diode time constant for different diameter size devices at various current densities. (b) Carrier escape time constant.

$$\frac{v_{out}}{v_{in}} = \frac{\frac{R_w}{R_s + R_c}}{(1 + j\omega\tau_{rec}) \left(1 + j\omega \frac{R_s}{R_s + R_c} \tau_0 \right) + \frac{R_w}{R_s + R_c} (1 + j\omega R_s C_{tot})}. \quad (15)$$

There are three elements in the denominator of Eq. (15) which contribute to the LED bandwidth. $(1 + j\omega\tau_{rec})$ is related to carrier recombination, $\left(1 + j\omega \frac{R_s}{R_s + R_c} \tau_0\right)$ depends on diode parameters and device parasitic elements, and $\frac{R_w}{R_s + R_c} (1 + j\omega R_s C_{tot})$ is a combination of both. Two resistance ratios, $\frac{R_s}{R_s + R_c}$ and $\frac{R_w}{R_s + R_c}$, affect the modulation response at different current densities. To better understand their role in the modulation response, their values are plotted for different device sizes at various current densities in Fig. 8. We note that the parameters in the numerator of Eq. (15) normalize out and do not affect the modulation bandwidth.

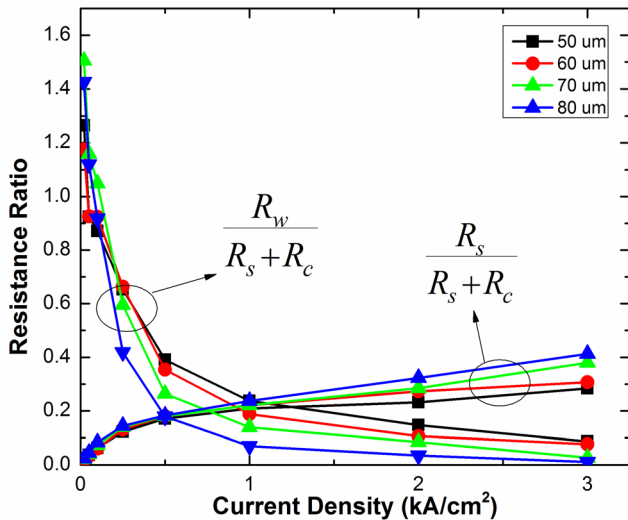


FIG. 8. Resistance ratios from the modulation response of Eq. (15) vs. current density.

At very low current densities, $\frac{R_s}{R_s + R_c}$ is very small due to the significant value of R_c resulting from the small population of unconfined carriers in the cladding region, causing $\left(1 + j\omega \frac{R_s}{R_s + R_c} \tau_0\right) \approx 1$. Therefore, the modulation response of Eq. (15) at low current densities can be approximated as

$$\frac{v_{out}}{v_{in}} \approx \frac{\frac{R_w}{R_s + R_c}}{(1 + j\omega\tau_{rec}) + \frac{R_w}{R_s + R_c} (1 + j\omega R_s C_{tot})}. \quad (16)$$

Based on the results of Subsecs. IV A and IV B, $R_s C_{tot}$ is very small compared to τ_{rec} and the modulation response may be further approximated by assuming $R_s C_{tot} \approx 0$

$$\frac{v_{out}}{v_{in}} \approx \frac{\frac{R_w}{R_s + R_c + R_w}}{\left(1 + j\omega \frac{R_s + R_c}{R_s + R_c + R_w} \tau_{rec}\right)}. \quad (17)$$

Based on Eq. (17), the modulation response of the LED at low current densities can be approximated as a single pole function. Although it is very common among researchers to assume the modulation response is only governed by recombination, Eq. (17) shows it also depends on carrier capture and diffusion processes (R_c) as well as the parasitic resistance of the device (R_s). Later, this difference will be shown by comparing Eqs. (17) and (18) in the low current density regime. Equation (18) shows the simplest form of the modulation response of an LED, considering only the recombination process as responsible for the modulation bandwidth

$$\frac{v_{out}}{v_{in}} \approx \frac{\frac{R_w}{R_s + R_c + R_w}}{(1 + j\omega\tau_{rec})}. \quad (18)$$

Similarly, at high current densities $\frac{R_w}{R_s + R_c}$ is very small due to a large population of carriers in the QW lowering the resistance (R_w), while $\frac{R_s}{R_s + R_c}$ is considerable, allowing Eq. (15) to be approximated as

$$\frac{v_{out}}{v_{in}} \approx \frac{\frac{R_w}{R_s + R_c}}{(1 + j\omega\tau_{rec}) \left(1 + j\omega \frac{R_s}{R_s + R_c} \tau_0\right)}. \quad (19)$$

The approximate form of the modulation response in Eq. (19) is of interest because it represents the transfer function of a two-pole system. This shows that the frequency bandwidth of the LED at high current densities not only depends on the carrier recombination lifetime but also on parameters related to device area, contact quality, doping level,

mobility, carrier diffusion, and capture. These parameters combine in the RC time constant as $\tau_{RC} = \frac{R_s}{R_s + R_c} \tau_0$, where again $\tau_0 = R_c(C_c + C_{sc})$.

Figure 9 shows a comparison of the modulation response re-constructed from the approximations discussed above in order to compare the applicable range of the different approximations. Data from a 70 μm diameter device at three current densities of 20 A/cm², 0.5 kA/cm², and 3 kA/cm² functioning as low, moderate, and high current densities, respectively, were used to study the approximations. Figure 9(a) shows that at low current densities (20 A/cm²), Eqs. (16) and (17) are good approximations to Eq. (15), which is the exact model for modulation response. Equations (18) and (19) are also considerably different than Eq. (17) and the exact expression of the modulation response. This shows that the modulation bandwidth of the LED at low current densities is strongly affected by diffusion and capture of carriers as well as parasitic effects. Therefore, consideration of recombination as the only process responsible for the bandwidth brings significant inaccuracies to the results. Figure 9(b) shows a comparison of these approximations at a current density of 0.5 kA/cm². For this moderate current density regime, none of the approximations represent the exact form of the function perfectly. However, at the high current densities shown in Fig. 9(c), the two-pole function of Eq. (19) is a good approximation to the exact form of the modulation response in Eq. (15), while the other approximations fail to replicate the exact response at high frequencies.

Figure 10 shows that the RC time constant τ_{RC} (~ 0.1 ns) is much shorter than τ_{rec} (~ 1 ns) for these devices and higher for larger diameters, as expected. The short RC time constant shows that the frequency modulation bandwidth at high current densities is mainly limited by the differential carrier lifetime in the present micro-LEDs with diameters below 100 μm . However, for active region designs with shorter differential carrier lifetimes or for LEDs with larger diameters, the RC time constant and carrier lifetime will approach the same order of magnitude, making the consideration of RC characteristics critical in predicting the bandwidth performance.

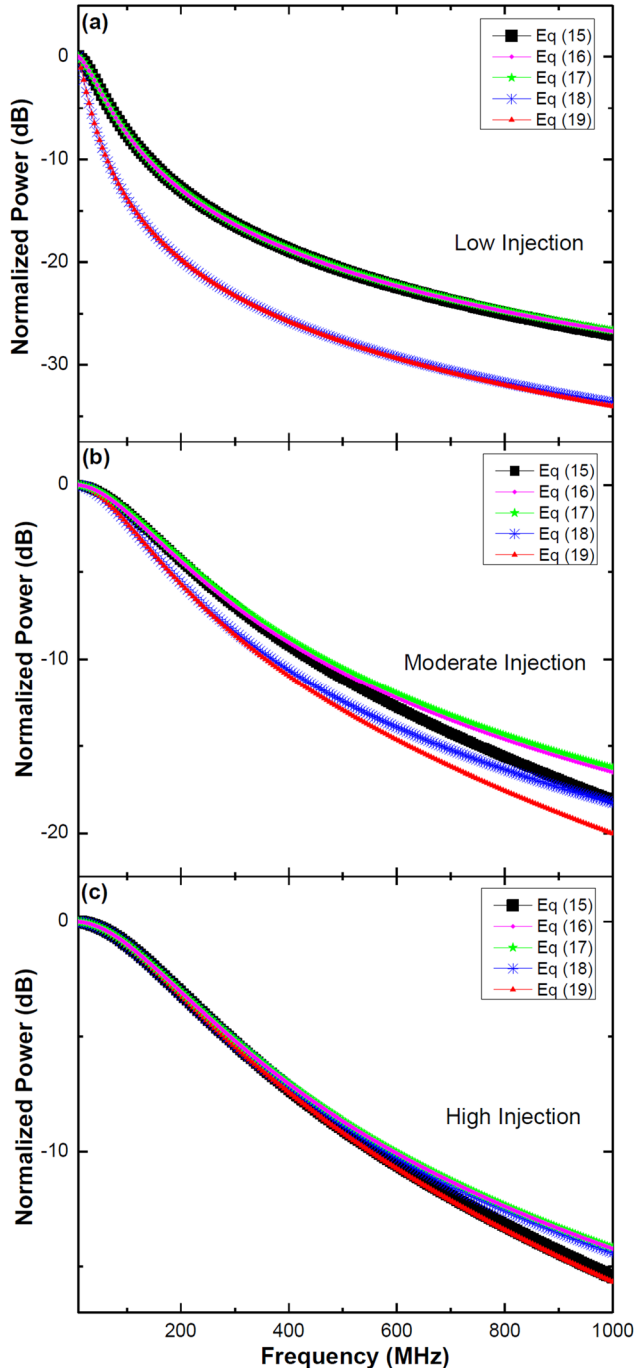


FIG. 9. Different approximations to the complete modulation response of the LED [Eq. (15)] for a 70 μm diameter device at (a) 20 A/cm², (b) 0.5 kA/cm², and (c) 3 kA/cm².

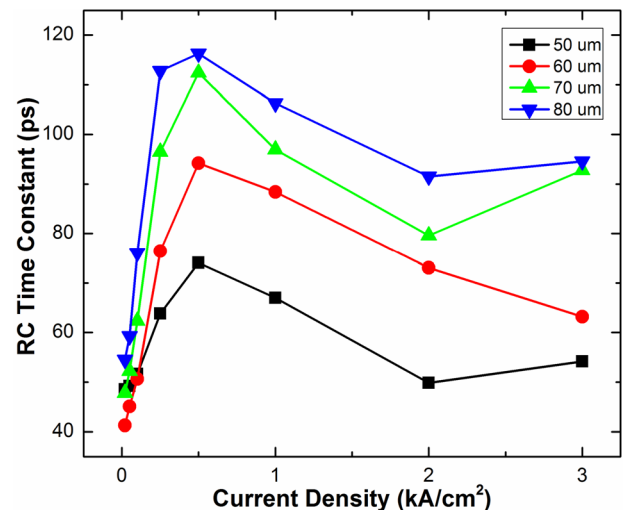


FIG. 10. RC time constant of different sizes at various current densities.

V. CONCLUSION

In this work, we have introduced an accurate method to study the carrier dynamics and transport effects in electrically injected III-nitride LEDs. This method uses small-signal rate equations considering both the recombination process and transport effects to derive the small-signal equivalent circuit of the device. By fitting the derived circuit to the impedance and modulation responses of the device, the differential carrier lifetime and transport related parameters were determined. Nonpolar MQW InGaN/GaN LEDs with circular diameters of 50, 60, 70, and 80 μm were studied to substantiate the method. Finally, we derived approximations for the modulation response under low and high injection levels and show that the transport of carriers affects the modulation response of the device, especially at low injection levels. Decoupling the effects of transport and recombination on the modulation response is important to establish device designs with low RC time constant and short recombination lifetime, which are both needed for high-speed VLC applications.

ACKNOWLEDGMENTS

This work was supported by the Department of Defense under Award No. W911NF-15-1-0428.

- ¹H. Haas, L. Yin, Y. Wang, and C. Chen, *J. Lightwave Technol.* **34**, 1533 (2016).
- ²H. Chun, S. Rajbhandari, G. Faulkner, D. Tsonev, E. Xie, J. J. D. McKendry, E. Gu, M. D. Dawson, D. C. O'Brien, and H. Haas, *J. Lightwave Technol.* **34**, 3047 (2016).
- ³Y. Wang, L. Tao, X. Huang, J. Shi, and N. Chi, *IEEE Photonics J.* **7**, 7904507 (2015).
- ⁴J. Zubia and J. Arrue, *Opt. Fiber Technol.* **7**, 101 (2001).
- ⁵E. Rosenkrantz and S. Armon, *Proc. SPIE* **9224**, 922413 (2014).
- ⁶J.-W. Shi, K.-L. Chi, J.-M. Wun, J. E. Bowers, Y.-H. Shih, and J.-K. Sheu, *IEEE Electron Device Lett.* **37**, 894 (2016).
- ⁷R. X. Ferreira, E. Xie, J. J. McKendry, S. Rajbhandari, H. Chun, G. Faulkner, S. Watson, A. E. Kelly, E. Gu, and R. V. Penty, *IEEE Photonics Technol. Lett.* **28**, 2023 (2016).
- ⁸J.-W. Shi, J.-K. Sheu, C.-H. Chen, G.-R. Lin, and W.-C. Lai, *IEEE Electron Device Lett.* **29**, 158 (2008).
- ⁹A. Rashidi, M. Monavarian, A. Aragon, S. Okur, M. Nami, A. Rishinaramangalam, S. Mishkat-Ul-Masabih, and D. Feezell, *IEEE Photonics Technol. Lett.* **29**, 381 (2017).
- ¹⁰S. Rajbhandari, J. J. McKendry, J. Herrnsdorf, H. Chun, G. Faulkner, H. Haas, I. M. Watson, D. O'Brien, and M. D. Dawson, *Semicond. Sci. Technol.* **32**, 023001 (2017).
- ¹¹W. Yang, S. Zhang, J. J. McKendry, J. Herrnsdorf, P. Tian, Z. Gong, Q. Ji, I. M. Watson, E. Gu, and M. D. Dawson, *J. Appl. Phys.* **116**, 044512 (2014).
- ¹²J. Iveland, L. Martinelli, J. Peretti, J. S. Speck, and C. Weisbuch, *Phys. Rev. Lett.* **110**, 177406 (2013).
- ¹³M.-H. Kim, M. F. Schubert, Q. Dai, J. K. Kim, E. F. Schubert, J. Piprek, and Y. Park, *Appl. Phys. Lett.* **91**, 183507 (2007).
- ¹⁴A. David and M. J. Grundmann, *Appl. Phys. Lett.* **96**, 103504 (2010).
- ¹⁵M. R. Krames, O. B. Shchekin, R. Mueller-Mach, G. O. Mueller, L. Zhou, G. Harbers, and M. G. Craford, *J. Disp. Technol.* **3**, 160 (2007).
- ¹⁶M. H. Crawford, *IEEE J. Sel. Top. Quantum Electron.* **15**, 1028 (2009).
- ¹⁷H. Kim, D.-S. Shin, H.-Y. Ryu, and J.-I. Shim, *Jpn. J. Appl. Phys., Part 1* **49**, 112402 (2010).
- ¹⁸M. Minsky, S. Fleischer, A. Abare, J. Bowers, E. Hu, S. Keller, and S. DenBaars, *Appl. Phys. Lett.* **72**, 1066 (1998).
- ¹⁹M. Pophristic, F. Long, C. Tran, I. Ferguson, and R. Karlicek, Jr., *Appl. Phys. Lett.* **73**, 3550 (1998).
- ²⁰I. Reklaitis, F. Nippert, R. Kudźma, T. Malinauskas, S. Karpov, I. Pietzonka, H. Lugauer, M. Strassburg, P. Vitta, and R. Tomašiūnas, *J. Appl. Phys.* **121**, 035701 (2017).
- ²¹S. Okur, M. Nami, A. K. Rishinaramangalam, S. H. Oh, S. P. DenBaars, S. Liu, I. Brener, and D. F. Feezell, *Opt. Express* **25**, 2178 (2017).
- ²²G. Shtengel, D. Ackerman, and P. Morton, *Electron. Lett.* **31**, 1747 (1995).
- ²³D. F. Feezell, M. C. Schmidt, S. P. DenBaars, and S. Nakamura, *MRS Bull.* **34**, 318 (2009).
- ²⁴L. A. Coldren, S. W. Corzine, and M. L. Mashanovitch, *Diode Lasers and Photonic Integrated Circuits*, 2nd ed. (John Wiley & Sons, 2012), p. 257.
- ²⁵A. David and M. J. Grundmann, *Appl. Phys. Lett.* **97**, 033501 (2010).
- ²⁶P. G. Eliseev, M. Osin'ski, H. Li, and I. V. Akimova, *Appl. Phys. Lett.* **75**, 3838 (1999).
- ²⁷J. Müller, M. Scheubeck, M. Sabathil, G. Brüderl, D. Dini, S. Tautz, T. Lerner, A. Breidenassel, and S. Lutgen, *Appl. Phys. Lett.* **96**, 131105 (2010).
- ²⁸T. Lee, *Bell Labs Tech. J.* **54**, 53 (1975).
- ²⁹R. Nagarajan, M. Ishikawa, T. Fukushima, R. S. Geels, and J. E. Bowers, *IEEE J. Quantum Electron.* **28**, 1990 (1992).
- ³⁰R. Tucker and D. Pope, *IEEE J. Quantum Electron.* **19**, 1179 (1983).
- ³¹L. Riuttanen, P. Kivisaari, N. Mäntyoja, J. Oksanen, M. Ali, S. Suihkonen, and M. Sopanen, *Phys. Status Solidi C* **10**, 327 (2013).
- ³²F. Nippert, S. Karpov, I. Pietzonka, B. Galler, A. Wilm, T. Kure, C. Nenstiel, G. Callsen, M. Straßburg, and H.-J. Lugauer, *Jpn. J. Appl. Phys., Part 1* **55**, 05FJ01 (2016).
- ³³A. David, C. A. Hurni, N. G. Young, and M. D. Craven, *Appl. Phys. Lett.* **109**, 033504 (2016).
- ³⁴I. Esquivias, S. Weisser, B. Romero, J. Ralston, and J. Rosenzweig, *IEEE J. Quantum Electron.* **35**, 635 (1999).
- ³⁵H. Hirayama, J. Yoshida, Y. Miyake, and M. Asada, *IEEE J. Quantum Electron.* **30**, 54 (1994).
- ³⁶J. Lee, M. Vassell, and G. Jan, *IEEE J. Quantum Electron.* **29**, 1469 (1993).
- ³⁷J. Vlach, *Linear Circuit Theory: Matrices in Computer Applications* (CRC Press, 2014).
- ³⁸D. Feezell, R. Farrell, M. Schmidt, H. Yamada, M. Ishida, S. DenBaars, D. Cohen, and S. Nakamura, *Appl. Phys. Lett.* **90**, 181128 (2007).
- ³⁹M. Meneghini, N. Trivellin, G. Meneghesso, E. Zanoni, U. Zehnder, and B. Hahn, *J. Appl. Phys.* **106**, 114508 (2009).
- ⁴⁰B. Deveaud, J. Shah, T. Damen, and W. Tsang, *Appl. Phys. Lett.* **52**, 1886 (1988).